Available online at www.sciencedirect.com

jmr&t Journal of Materials Research and Technology

journal homepage: www.elsevier.com/locate/jmrt

Original Article

Property degradation of seawater sea sand cementitious mortar with GGBFS and glass fiber subjected to elevated temperatures

Fulin Qu [a], *Wengui Li* [a,*], *Zhuo Tang* [a], *Kejin Wang* [b]

[a] School of Civil and Environmental Engineering, University of Technology Sydney, NSW 2007, Australia
[b] Department of Civil, Construction and Environmental Engineering, Iowa State University, IA 50011, USA

ARTICLE INFO

Article history:
Received 10 February 2021
Accepted 25 April 2021
Available online 30 April 2021

Keywords:
Cementitious mortar
Seawater
Elevated temperature
Ground granulated blast-furnace slag (GGBFS)
Glass fiber
Sea sand

ABSTRACT

Effects of ground granulated blast-furnace slag (GGBFS) and glass fiber on the property degradation of seawater sea sand mortar (FSSM) after elevated temperature exposure were investigated in this study. The physical properties and mechanical strength of FSSM were compared with that of cementitious mortar prepared with demineralized water and river sand (FRRM). The results showed that when the mortars were exposed to normal temperature, the compressive strength of FSSM was higher than that of FRRM. GGBFS increased both the compressive and flexural strengths of FSSM, while glass fiber increased the flexural strength but slightly decreased the compressive strength. The maximum flexural strength of FSSM was achieved with 1 wt.% glass fiber and 30% GGBFS. After exposed to temperatures of 200 °C and 400 °C, the flexural and compressive strength losses of FSSM were lower than that of the corresponding FRRM, while the FSSM with glass fiber exhibited more compressive strength loss but less flexural strength loss compared to the FRRM. Additionally, GGBFS could densify the microstructure of FSSM, and decrease the losses of flexural and compressive strength after exposed to elevated temperatures. The calcium aluminosilicate hydrate (C–A–S–H) gels with higher ratios of Si/Ca and Al/Ca in the FSSM with GGBFS were significantly more stable at the temperature of 700 °C compared to the calcium silicate hydrate (C–S–H) gels with lower ratios of Si/Ca and Al/Ca in the FRRM or FSSM without GGBFS. Therefore, it can be included that the high temperature or fire resistance of FSSM can be improved by glass fibers and GGBFS.

1. Introduction

Recently cementitious materials, manufactured with freshwater and river sand, are one of the most widely-used buildings and structural materials worldwide for their versatility and economy. It is predicted that there might be a shortage of freshwater and river sand in the 21st century [1,2]. The use of seawater, instead of freshwater in concrete, can be a sustainable way to protect freshwater sources from overuse. Similarly, the use of sea sand without desalting is also the latest development trend for releasing the burden of depleted

* Corresponding author.
E-mail address: wengui.li@uts.edu.au (W. Li).
https://doi.org/10.1016/j.jmrt.2021.04.068

river sand sources. Although high-salt content seawater/unwashed sea sand has been prohibited in reinforced concrete for many years due to steel corrosion, non-corrosive steel such as fiber-reinforced polymers (FRP) could make the application of seawater and sand in low-cost and long-life concrete become a reality [3–5]. In addition, fire or high temperature is an extreme environmental condition to which any building or structure could be exposed during its service life [6–9]. Concrete buildings and structures adopting the seawater and unwashed sea sand as the raw materials are also supposed to have significant performance under extreme fire conditions.

Up to now, various studies have evaluated the performance of ordinary Portland cement concrete (OPC) after high-temperature exposure [10–15]. The composition of OPC, including aggregate and cement paste, can be affected by the increasing temperature since the OPC is a heterogeneous building material [10–12]. OPC's performance under fire environments lies in its ingredient and the characteristics of its elements. The hydration product of OPC, such as Portlandite (CH), can decompose to form calcium oxide and release water at approximately 400 °C–500 °C. Under fire conditions, phase changes, pore pressure changes, and the limited thermal conductivity in OPC could significantly affect the mechanical properties [13]. When the temperature exceeds 400 °C, the strength is practically lost, as the result of the dehydration of CH and rehydration of CaO [14]. The strength loss of OPC exceeds 50% when exposure temperatures are up to around 400 °C–500 °C due to the dehydroxylation of hydroxide and constant dehydration of calcium silicate hydrate (C–S–H) starting at 105 °C [15]. OPC could be suffered wide-ranging damage due to physical and chemical changes at high temperatures, leading to severe deterioration of mechanical performances [6–9]. Therefore, some researchers have explored the possibility of adjusting the concrete ingredients to provide a more stable microstructure of the cement-base composites.

Incorporating glass fibers as reinforcing agents is one of the most efficient methods to optimize the microstructure of the cement-based composites, especially when the structure is needed to consider to carry tension load, for the fact that the increase of elastic tension will cause great microcracks and integrated rupture of unenhanced matrix [16]. The quality of glass fibers was guaranteed by some glass technologies mentioned in previous references [17–20]. The application of glass fibers in this concrete structure can protect the physical and also chemical characteristics of fibers and their surroundings [21,22]. Glass fibers are able to be recognized as the primary load-carrying component [23,24]. The matrix of cement-based composites encircling fiber is prohibiting them from being affected by the surrounded environment. Besides, glass fibers can also be seen as the load transducers that enable the fibers to move steadily within them [23,24]. Immensely, adequate fibers in the composite matrix can comfortably improve tensile strength. Besides, it is reasonable to select the glass fibers to optimize the cement-based composites' microstructure for their beneficial physical characteristics and comparatively cheap cost [25]. The glass fibers have also been reported to play an essential role in prohibiting the formation of cracks in the cement-based composites under a fire environment for the high melt point of glass fibers [26,27]. Besides, a large number of investigations have been conducted to confirm the feasibility of using industrial by-products such as ground granulated blast-furnace slag (GGBFS) to provide a more stable microstructure in cement-based composites or GGBFS-based cementitious materials [28–32]. Aziz et al. reported that a reduction in the number of pores in alkali-activated slag after exposure to elevated temperatures [33]. Delhomme et al. [34] studied the influence of high temperature on cement mortar with substitutes of GGBFS and concluded that an increase of GGBFS content to 20% or above significantly promoted the fire resistance at the water to bind ratio of 0.6. Gao et al. [35] investigated the splitting strength of OPC and high-strength pozzolanic concretes at high temperatures and illustrated that pozzolanic concrete containing GGBFS had better performance than the OPC.

Most studies on seawater and sea-sand cement-based composites focused on the influence of hydration reaction and FRP-reinforced concrete structural performance [3–5,36–39]. Li et al. [40] only investigated the thermal and mechanical properties of geopolymer mortar mixed with seawater and sea sand and concluded that the seawater and sea sand have a slightly detrimental effect on the residual strength of geopolymer mortar. Limited studies have been conducted to investigate cement-based composite fire resistivity utilizing seawater and sea sand [37–39]. Therefore, the aim of this study is to investigate the effect of GGBFS and glass fiber on the thermal performance and flexural behaviors of seawater and sea-sand mortars (FSSM) to provide a more stable microstructure. The mortars mixed with demineralized water and river sand (FRRM) were also manufactured as the reference group. The mass loss, visual appearance, compressive and flexural strength were investigated in this study. In order to explain the differences (between FRRM and FSSM) caused by sea sand and seawater, the improvement of the combined GGBFS and glass fiber, the change of microstructure and hydration products was measured by using various techniques, including X-ray diffraction (XRD), Fourier transforms infrared spectroscopy (FTIR), thermogravimetric analysis (TGA), and backscatter electrons (BSE) with energy dispersive X-ray (EDX). It is expected that the results of this study will contribute to the development of new construction materials that perform well at high temperatures.

2. Materials and specimen preparation

2.1. *Raw materials*

The mortar was manufactured based on the Eureka general-purpose cement in accordance with AS/NZS 2350.1-2006 (Methods of testing Portland, blended and masonry cements sampling) and GGBFS in accordance with the AS 3582.2:2014 (Supplementary cementitious materials Slag – Ground granulated blast-furnace) as binding materials. Two types of water, demineralized water, and seawater, were applied as the mixing water. Two types of sand (river sand and sea sand) were employed as fine aggregates. The seawater and sea sand were obtained from the Botany Bay near Sydney, Australia,

Table 1 – Chemical properties of composition of cement, GGBFS and sea sand, and mineral properties of cement.

Chemical properties (by weight %)								
Type	SiO_2	Al_2O_3	Fe_2O_3	CaO	MgO	SO_3	Na_2Oeq	K_2O
Cement	21.8	4.5	3.5	65.4	2.6	1.4	0.6	1.3
GGBFS	36.0	11.8	0.3	42.6	5.8	0.5	0.2	0.3
Sea sand	96.5	0.21	0.43	1.3	0.1	0.01	0.07	0.05
Mineral properties of cement (by weight %)								
C_3S	C_2S	C_3A	C_4AF	Blaine	Density		Water demand	
54%	14%	7%	11%	357 m^2/kg	3.06 g/cm^3		28.0%	

and the sea sand mentioned in the following section was all the sea sand without desalting.

The Blaine, density, and specific gravity of GGBFF were 418 m^2/kg, 1.28 g/cm^3 and 2.92, respectively. The primary chemical composition of cement, GGBFS, and sea sand measured by X-ray fluorescence (XRF) is listed in Table 1. The mineral composition and physical properties of cement are also listed in Table 1. Sieve analysis was carried out according to AS1141.11.1-2009 (Methods for sampling and testing aggregates – particle size distribution – sieving method) to determine the particle size distribution (PSD) of cement, GGBFS, river sand, and sea sand. The PSD curves of the materials used are compared in Fig. 1. The fineness modulus of river sand was 2.39, and that of sea sand was 1.86, indicating the river sand was slightly coarser than the sea sand. The chemical composition of the seawater and sea sand by inductively-coupled plasma mass spectrometry is displayed in Table 2. There were high chloride and sulfate ions content in seawater and relatively low weight percentage of chloride and sulfate in sea sand, while no chloride content was founded in river sand and demineralized water.

A kind of commercial compound glass fiber with 12 mm in length and 33 μm in diameter was also used in this experiment. The density of the glass fiber used in this study was 0.91 g/cm^3. The melting point is around 270 °C. Glass fiber-reinforced FSSM mortars were manufactured with 1.0 wt.% of the total mass. The furnace test was adopted to identify physical evolutions of glass fiber after high-temperature

Table 2 – Chemical compositions in seawater and sea sand from Botany Bay (Sydney, Australia).

Concentration (g/l)	NaCl	$MgCl_2$	Na_2SO_4	KCl	$CaCl_2$	$NaHCO_3$
Seawater	19.0	1.35	0.88	0.38	0.40	–
Salt content (wt.%)		Cl			SO_4	
Sea sand		0.83			0.09	

exposure [41]. The same quantities of glass fibers were held in a quartz crucible and then put into a furnace oven with the heating rate of 10 °C/min, and kept for two hours until the temperature was up to the different target temperatures (200 °C, 400 °C, and 700 °C), and finally, the mass change and physical transformations for the glass fibers were recorded in Fig. 2. There were indeed some noticeable changes in the physical properties of glass fiber after different high-temperature exposure. There was no mass change of glass fibers after exposure to 200 °C; in contrast, there were 20% and 50% mass loss after being exposed to 400 °C and 700 °C, respectively, indicating that the glass fiber could be partially melted in 400 °C and 700 °C.

2.2. *Mix design*

Four series of cement mortar mixes with seawater and sea sand were studied: cement mortar mixes only with seawater

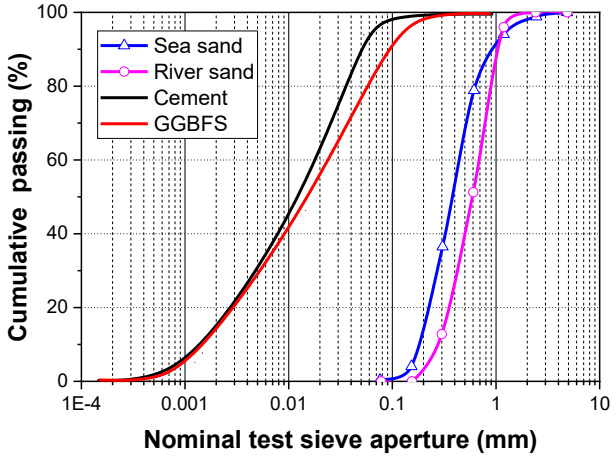

Fig. 1 – Particle size distribution curves of raw materials used.

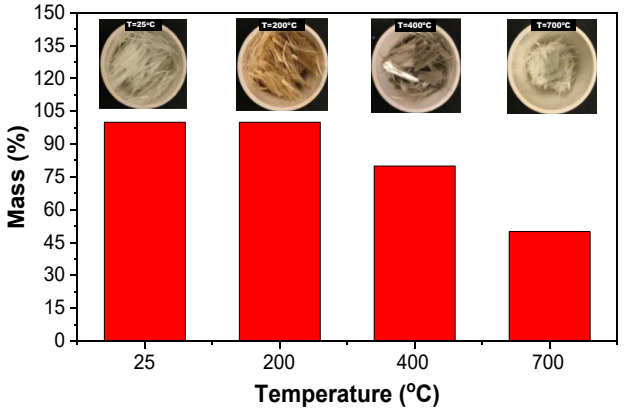

Fig. 2 – Physical transformations and mass change of glass fiber after the furnace test under different heating temperatures.

Table 3 – Mix proportion design of cement mortars (gram).

Sample	Cement	Demineralized water	Seawater	River sand	Sea sand	GGBFS	Glass fiber	SP
FRRM	300	90	–	600	–	–	–	–
FSSM	300	–	90	–	600	–	–	–
FSSM-1F	300	–	90	–	600	–	9.9	1.8
FSSM-10S	270	–	90	–	600	30	–	–
FSSM-20S	240	–	90	–	600	60	–	–
FSSM-30S	210	–	90	–	600	90	–	–
FSSM-10S-1F	270	–	90	–	600	30	9.9	1.8
FSSM-20S-1F	240	–	90	–	600	60	9.9	1.8
FSSM-30S-1F	210	–	90	–	600	90	9.9	1.8

and sea sand, FSSM mixes with 1 wt.% glass fiber (FSSM-F group, named FSSM-1F), FSSM mixes with 10, 20, and 30 wt.% GGBFS substitutes for cement (FSSM-GGBFS group, named FSSM-10S, FSSM-20S, and FSSM-30S, respectively), and FSSM mixes with GGBFS substitutes and glass fiber (FSSM-GGBFS-F group, named FSSM-10S-1F, FSSM-20S-1F, and FSSM-30S-1F, respectively). The mortar mixed with demineralized and river sand was also cast as the reference group. All mixes had a 0.30 ratio of water to binder (W/B) and a 2.0 ratio of binder to sand. 0.6% superplasticizer (SP) was added to the group with the addition of glass fiber. All mortar mixes proportions are illustrated in Table 3.

2.3. *Specimen preparation*

Specimens with dimensions of 40 mm × 40 mm × 140 mm were fabricated according to ASTM C348-20 (Standard test method for flexural strength of hydraulic-cement mortars). All mortars with or without glass fiber were mixed based on the following procedure: sand was mixed with binder at a slow speed for 1 min. After the low-speed mix, the water or seawater with SP was put into the Hobart mixer, followed by another 2 min of slow mixing. After a 1 min rest, high-speed mixing was applied for 2 min. After this, for the non-fiber mixtures, they were cast into oiled moulds, while for the fiber-reinforced mixtures, the glass fiber was added into the mixtures along with SP and mixed for another 2-min at a high-speed and they were then cast into oiled moulds to form specimens. All mortars were kept for 1 day in a climate chamber with RH of 95% and a temperature of 20 ± 1 °C. After curing for 24 h, the mortars were demoulded and kept in the same curing conditions for the testing time.

3. Experimental program

3.1. *High-temperature exposure*

All surface-drying mortar specimens in one layer were exposed to the different target temperatures of 200 °C, 400 °C, and 700 °C with a heating rate of 5 °C/min [29]. After reaching a target temperature, they were maintained at the temperature for 2.5 h by employing a furnace oven, as shown in Fig. 3. Specimens were taken out from the furnace oven, cooled down to room temperature, and finally applied to the following experimental investigations.

3.2. *Physical properties*

A high-resolution camera recorded the visual appearance before and after high-temperature exposure of all mixes. Before and after high-temperature exposure, the mass of all mixtures was measured by a scale with an accuracy of 0.01 g. The mass loss percentage was calculated by the mass change of the corresponding specimens before and after high-temperature exposure compared to the mass before high-temperature exposure.

3.3. *Mechanical strengths*

After 28-day curing in the lab chamber and being exposed to high temperatures, three specimens of all mixtures were used for the flexural strength test by a universal testing machine in accordance with ASTM C348-20 (Standard test method for flexural strength of hydraulic-cement mortars). The fractured portions of the specimens after the flexural strength test were employed for a compressive strength test following ASTM C349-18 (Standard test method for compressive strength of hydraulic-cement mortars). The percentages of compressive and flexural strength loss were calculated based on the original strength and the strength loss caused by high temperature exposure.

3.4. *Microstructure characterization*

The fractured samples with the size of 2–5 mm and powder samples (pass through a 45 μm sieve), smashed from the core of mortars before and after high-temperature exposure were

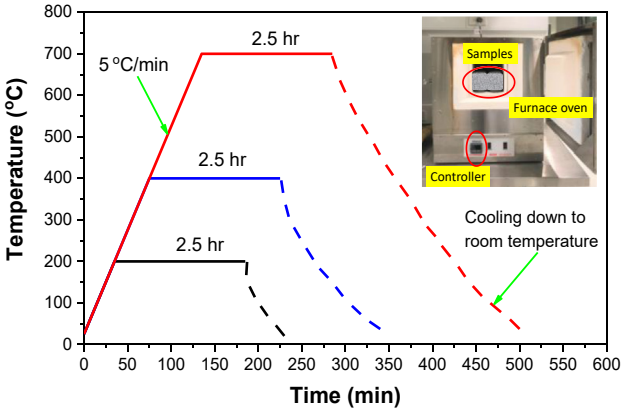

Fig. 3 – The time–temperature curve in the furnace oven.

used to investigate the change of microstructure and hydration products. To stop the cement hydration, the powder and fractured samples were soaked in 100% acetone. All soaked samples were then dried entirely within the drying oven at 40 °C for two days before being measured in the following test. The XRD analysis was employed to examine the composition evaluations occurring in all samples. The XRD analysis for powder samples was carried out by utilizing a BRUKER AXS D8 ADVANCE machine with 40 kV power and 40 mA in a Cu-Ka source. The tested angle of the 2θ was in the range from 5° to 70° at a step of 0.02°/min. The changing of molecular characterizations was measured by the FTIR analysis. The FTIR analysis for powder samples was performed with an attenuated total reflectance attachment for spectra measurement between 400 and 4000 cm^{-1} wavenumber at 8 cm^{-1} resolution.

Thermogravimetric analyses were conducted on powder samples to evaluate the alterations of the hydration reaction products for mortars before and after being subjected to elevated temperatures. The TGA analysis for powder samples was conducted by the application of the NETZSCH STA 449 machine in a nitrogen environment. The powder samples were maintained around 40 °C for 0.5 h and then heated from 40 °C to 1000 °C at a rate of 10.0 °C/min in the N_2 environment. The microstructure and composition change of hydration products in fractured samples were implemented by Zeiss Supra 55VP Backscatter electrons and energy dispersive X-ray with Raith Elphy Plus E-beam Lithography System as chemical composition analyzer at an accelerating voltage of 15 keV. After drying in the oven at 40 °C for two days, the lumpy samples were cured in epoxy resin, then polished with abrasive paper p300, p600, and p1200 by a grinder, and finally polished with 0.3 nm diamond polishing agent for approximately 10 min. The samples were carbon-coated for BSE-EDX analysis. The analytical process was set up to analyze the following elements: Al, Si, Cl, S, Na, and Ca. The chemical components were analyzed by Aztec 2.0 in accordance with the EDX results.

4. Results and discussions

4.1. *Physical properties*

The mass loss of all groups after high-temperature exposure is presented in Fig. 4. The mass of all groups increased with increasing temperature. At all high temperatures, the mass loss of the FRRM group was higher than that of FSSM, which might be related to the influence of seawater and sea sand on the hydration reaction. The addition of 1.0 wt.% fiber clearly increased mass loss at all elevated, resulting in a higher percentage of mass loss of FSSM-1F than that of FSSM and FRRM. After exposure to a temperature of 700 °C, the percentage of mass loss for FSSM-1F, FSSM, and FRRM was 12.5%, 11.8%, and 12.0%, respectively. The mass loss of FSSM mixtures with GGBFS was less than that of the FSSM group and the corresponding FSSM-GGBFS-F group. The mass loss of the groups with GGBFS slightly decreased with the increasing addition of GGBFS. The combination of glass fiber and GGBSF decreased the mass loss. As displayed in Fig. 4, the mass loss of FSSM-10S-1F was lower than that of FSSM. These were mainly related to a denser microstructure in the groups with GGBFS than in the FSSM specimens. The glass fiber reduced the relative content of cementitious material in the same volume of samples, and the partial mass loss of glass fiber occurred in 400 °C and 700 °C, which might account for a higher mass loss in groups with glass fibers.

Fig. 5 displays the visual appearance of the specimens after exposure to a temperature of 700 °C. No apparent cracks were detected in the visual appearance of mortars after exposure to 200 °C and 400 °C. Thus, the visual appearance of all specimens at 200 °C and 400 °C is not displayed in Fig. 5. As shown in Fig. 5, more cracks were founded in FRRM than in FSSM after exposure to 700 °C. The alteration of moisture loss, evaporation, and decomposition of chemical structures for those specimens could occur as the increasing temperature could lead to more cracks. The cracks in the FSSM-GGBFS specimens were less than that in FSSM, and the cracks could be relatively decreased with the increasing addition of GGBFS. Both longitudinal and transverse cracks were detected in the FRRM, FSSM, and FSSM-GGBFS specimens compared with only longitudinal cracks detected in FSSM-1F, which indicated that the glass fiber could effectively prevent the formation of cracks caused by the elevated temperature. The combination of GGBFS and fiber could also indeed protect the formation of cracks at high temperatures, without apparent cracks founded in the FSSM-GGBFS-F specimens.

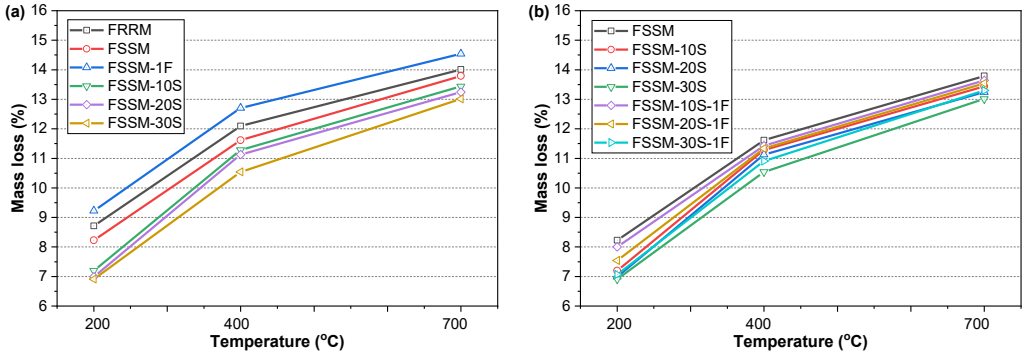

(a) FRRM, FSSM, FSSM-F, and FSS-GGBFS group (b) FSS-GGBFS and FSSM-GGBFS-F group

Fig. 4 – Mass loss of mortars after high-temperature exposures.

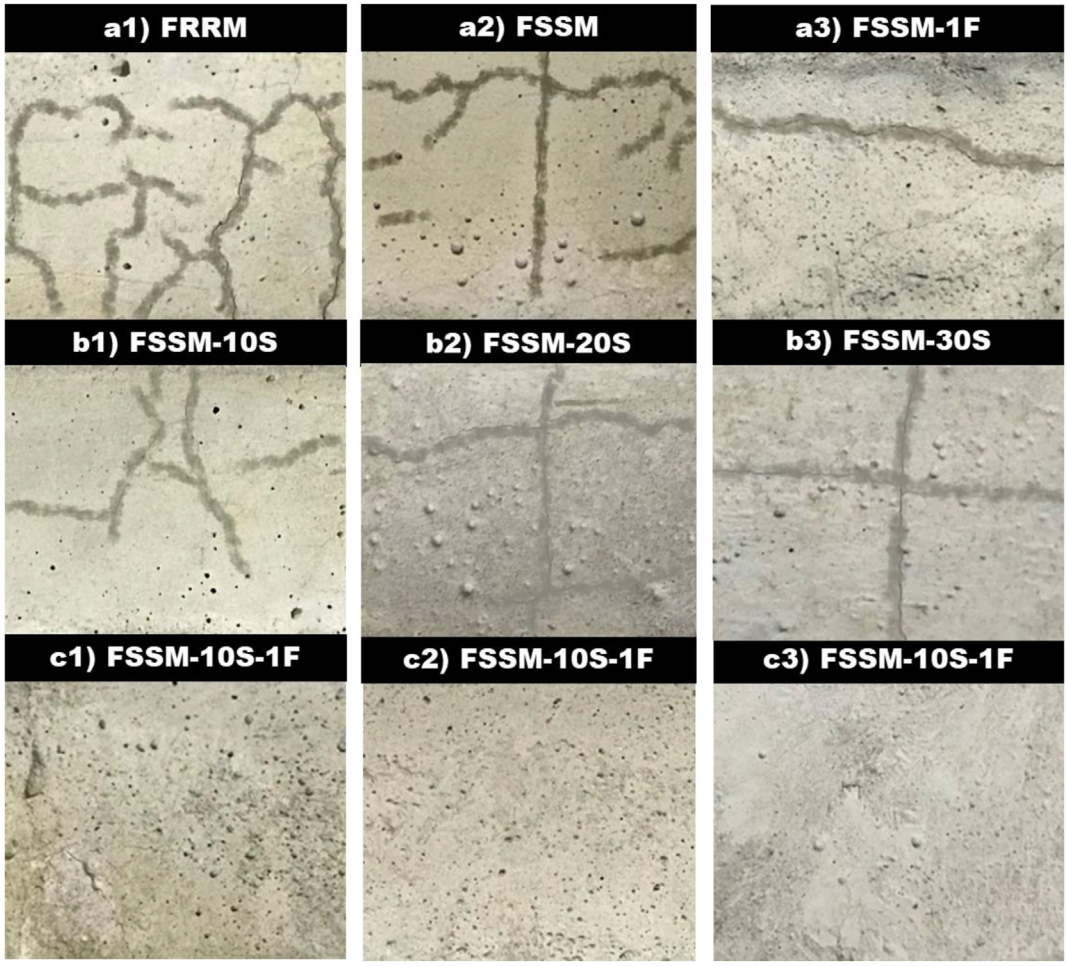

Fig. 5 – Visual appearance of all mortars after exposure to a temperature of 700 °C.

4.2. *Compressive and flexural strengths*

The compressive strength for all exposed and unexposed specimens and percentage of strength loss for all exposed specimens are illustrated in Fig. 6. For the compressive strength in Fig. 6(a), the compressive strength of FSSM was higher than that of FRRM, while FSSM-1F with the addition of fiber was lower than that of FRRM. The addition of GGBFS could increase the compressive strength of FSSM, and the increasing incorporation of GGBFS could also improve the compressive strength of the FSSM-GGBFS specimens. However, the compressive strength of the FSSM-F-GGBFS was lower than that of FSSM, which indicated that the compressive strength reduction caused by the addition of glass fiber was higher than the compressive strength increase due to the addition of GGBFS. As the temperature increased, the compressive strength was decreased, especially at 700 °C, a massive strength reduction of all groups could be founded. Similar differences in the compressive strength of all exposed specimens were examined and compared with those of unexposed specimens. For the compressive strength loss in Fig. 6(b), the FSSM-GGBFS group had the lowest strength loss followed by FSSM, FRRM, FSSM-GGBFS-F, and FSSM-F group at the temperature of 200 °C and 400 °C, while a higher compressive strength loss was founded in FRRM than those of FSSM-F and FSSM-GGBFS-F groups at 700 °C.

The flexural strength for all exposed and unexposed specimens and the percentage of flexural strength loss for all exposed specimens are illustrated in Fig. 7. The flexural strength of FSSM was lower than that of FRRM, which was related to the physical properties (low fineness modulus) of sea sand in the FSSM group [36]. The addition of fibers could increase the flexural strength of FSSM, resulting in a higher flexural strength of FSSM-1F than FRRM. The replacement of GGBFS for cement could also increase the flexural strength of FSSM, and the flexural strength of the FSSM-GGBFS group could also be increased with the increasing content of GGBFS. Although the flexural strength of FSSM-10S was lower than FRRM, the flexural strength of FSSM-20S and FSSM-30S was higher than that of FRRM. In addition, while the FSSM-30S had the highest flexural strength among the FSSM-GGBFS, the flexural strength of FSSM-30S was still lower than that of FSSM-1F, which indicated that the fiber had a higher ability to optimize the flexural strength than that of GGBFS. The

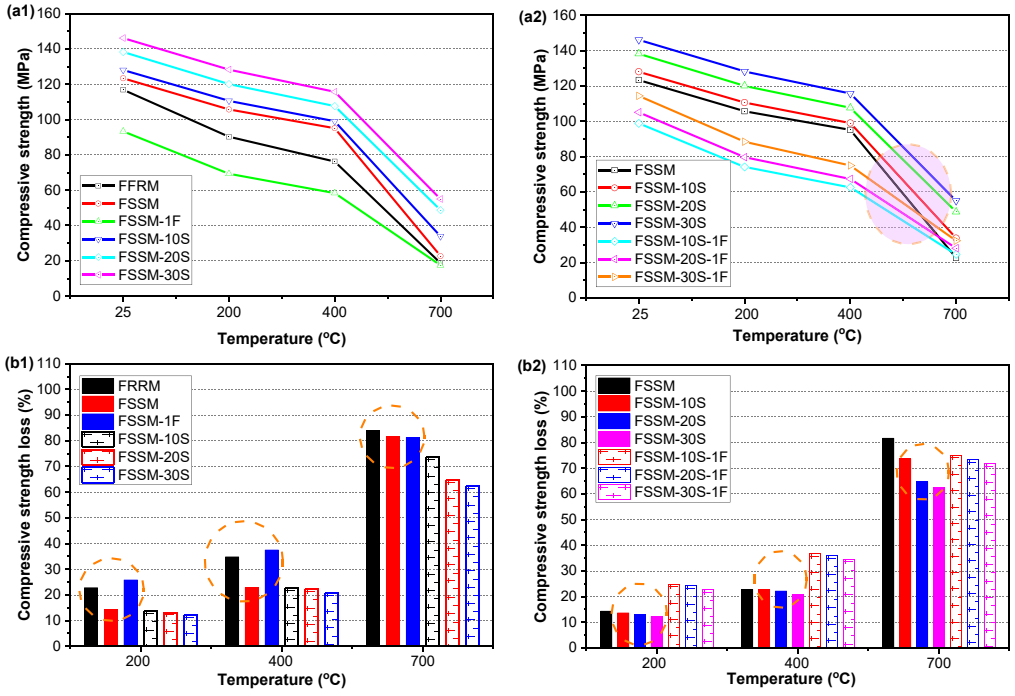

Fig. 6 – Effect of elevated temperature exposure on compressive strength: (a), Compressive strength of all unexposed and exposed groups; (b), Compressive strength loss after high-temperature exposure.

combination of fiber and GGBFS contributed to the highest flexural strength of FSSM-GGBFS-F. As the temperature increased, the flexural strength of all groups was decreased, especially a large amount of strength reduction of all specimens founded at 700 °C. Only the flexural strength of the FSSM-GGBFS-F could be recorded. The flexural strength changes of all exposed specimens were founded similarly with those of unexposed specimens, except the FRRM and FSSM after exposure to 400 °C. It should also be noted that the flexural strength in FRRM was higher than in FSSM at normal

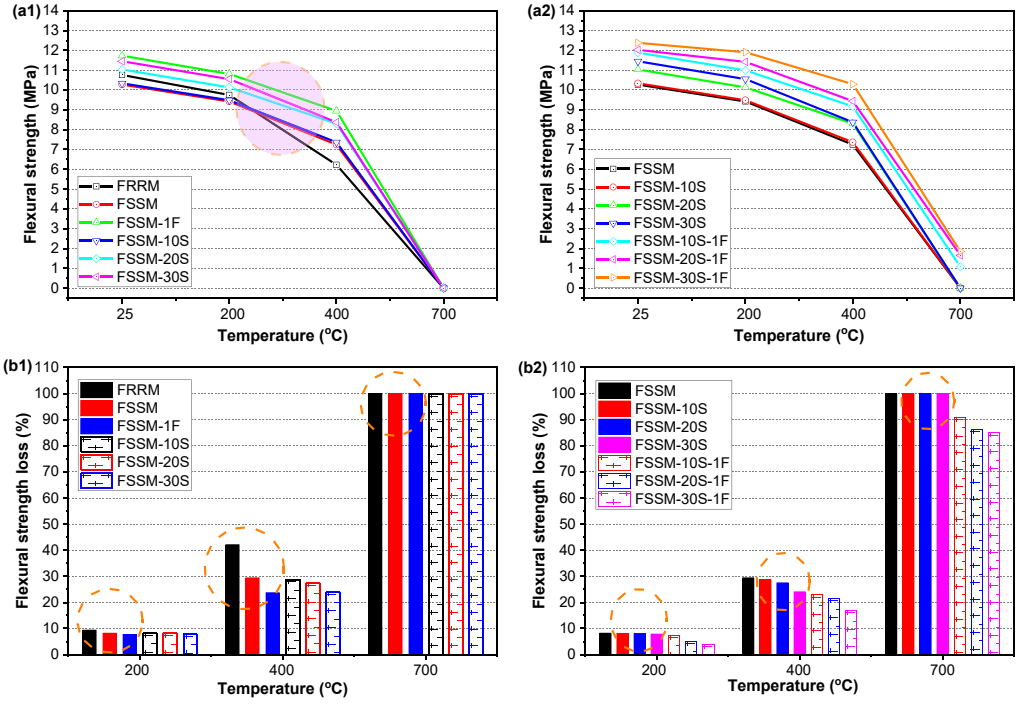

Fig. 7 – Effect of elevated temperature exposure on flexural strength. (a), Flexural strength of all unexposed and exposed specimens; (b), Flexural strength loss after high-temperature exposure.

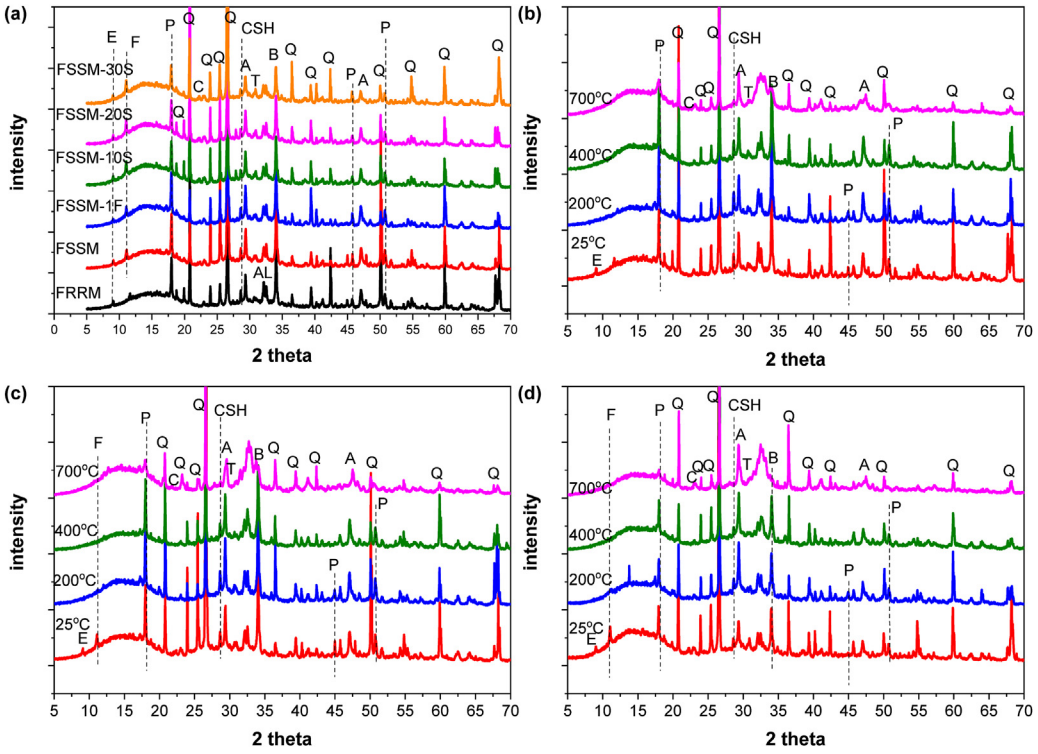

Fig. 8 – XRD diagrams for mortars before and after high-temperature exposures: (a) Comparison at 25 °C; (b) FRRM; (c) FSSM and (d) FSSM-30S. Peak labels are as follows: A-alite ($3CaO{\cdot}SiO_2$), AL – Aluminate, B-belite ($2CaO{\cdot}SiO_2$), CAF – Brownmillerite ($4CaO{\cdot}Al_2O_3{\cdot}Fe_2O_3$), C-calcite ($CaCO_3$), CSH ($3CaO{\cdot}2Al_2O_3{\cdot}3H_2O$), P-Portlandite ($Ca(OH)_2$), E-ettringite ($3CaO{\cdot}Al_2O_3{\cdot}CaSO_4{\cdot}12H_2O$), F- Friedel's salt ($3CaO{\cdot}Al_2O_3{\cdot}CaCl_2{\cdot}10H_2O$), Q-Quartz ($SiO_2$), and T-tri-calcium aluminate ($3CaO{\cdot}Al_2O_3$).

temperature and 200 °C, but lower than in FSSM at 400 °C, which indicated that there were some different microstructure changes between FRRM and FSSM groups. For the flexural strength loss in Fig. 7(b), the FSSM-GGBFS-F group had the lowest strength loss in all exposure temperatures, followed by FSSM-F, FSSM-GGBFS, FSSM, and FRRM groups. In addition, when the temperature was up to 700 °C, the percentage of flexural strength loss in all specimens except the FSSM-GGBFS-F group reached 100% because only the flexural strength of the FSSM-GGBFS-F group could be recorded.

In general, the seawater and sea sand could decrease the strength loss of FSSM, resulting in a lower strength loss of FSSM than that of FRRM in all exposure temperatures. The strength loss of FSSM could be decreased by the GGBFS and decreased with the increasing GGBFS. The addition of fiber had an adverse effect on the compressive strength of FSSM but had a positive effect on the flexural strength of FSSM. There are two possibilities for the addition of glass fiber to reduce the compressive strength of FSSM: glass fiber reduces the cement content of a given volume of mortar, and the interface between glass fiber and cement matrix may not be as strong as the interface between sand and cement [26,27]. The combination of GGBFS and fiber could optimize the microstructure of seawater sea-sand mortar, resulting in a lower flexural strength loss in the FSSM-GGBFS-F group after exposure to 700 °C.

4.3. *Microstructure characterization*

4.3.1. *X-ray diffraction*

The XRD results of all samples at 25 °C and the samples of FRRM, FSSM, and FSSM-30S after high-temperature exposure are displayed in Fig. 8. It showed the comparative XRD results in all samples before exposed to elevated temperatures. In Fig. 8(a), the data demonstrated that the all anhydrous test specimens before exposure to high temperatures were very similar to each other with the main clinker phase alite ($2\theta = 29.4$ and $47.0°$), belite ($2\theta = 34.0°$), tri-calcium aluminate ($2\theta = 29.9°$), quartz ($2\theta = 18.8, 19.8, 20.9, 23.9, 25.2, 26.8, 36.4, 39.3, 42.3, 50.0, 54.8, 59.9$ and $68.2°$), C–S–H ($2\theta = 28.7°$)and calcite ($2\theta = 22.3°$), as well as Portlandite ($2\theta = 18.0$ and $50.8°$). There were lots of intensity peaks of quartz due to the sand content in the mortar samples. There was still some unreacted cement paste in all samples identified by the appearance of the tri-calcium aluminate or belite. The main difference between the FRRM group and the FSSM group was that there was a high intensity of Kuzel's and Friedel's salt ($2\theta = 11.1°$) in the samples with seawater and sea sand, which might be related to the salt contents in seawater and sea sand [36]. The reason for accelerating cement hydration was primarily due to chloride promoting the precipitation of calcium, aluminate, and ferrite [36]. The peak of ettringite (AFt) at 9.09° 2θ was only founded in FRRM at 28 days. There was no big difference in the

XRD results between the FSSM and FSSM-1F mixes, indicating that the glass fiber had no major effect on the hydration reaction. In addition, the intensity of CH was decreased as the increasing GGBFS in the mixes with seawater and sea sand, indicating that there was a reaction between Portlandite and the chemical component in GGBFS [42].

Fig. 8(b)–(d) shows the comparative XRD results FRRM, FSSM, and FSSM-30S before and after high-temperature exposure. From the results of physical and mechanical properties, FSSM-30S performed best in the FSSM-GGBFS group. Therefore, after exposure to high temperatures, the discussion about the impact of GGBFS mainly focused on comparing FSSM-30S with other groups (the same below). At the temperature of 200 °C, there was only a noticeable reduction of the intensity for AFt in FRRM and a slight reduction of the intensity for Friedel's salt in FSSM and FSSM-30S, which indicated that the AFt and Friedel's salt could be partly decomposed under this temperature. When the temperature was up to 400 °C, there was a noticeable reduction of the intensity for AFt in the FRRM group and for Friedel's salt in FSSM and FSSM-30S systems, which indicated that the high temperature could significantly influence the AFt and Friedel's salt. Besides, after exposure to 700 °C, there was a noticeable reduction of the intensity for CH and C–S–H for all specimens. The FRRM had the most significant reduction of CH and C–S–H, followed by FSSM and FSSM-30S, which indicated that the FSSM and FSSM-GGBFS group was relatively lower influenced by the high temperature than that of FRRM. In addition, there was no significant change for the other phases, such as calcium, and quart indicating that these phases could be stable after high-temperature exposure, even up to 700 °C.

4.3.2. *Fourier transform infrared spectroscopy*

Fig. 9(a)–(d) shows the comparison of FTIR data (600–3700 cm^{-1}) among FRRM, FSSM, FSSM-1F, FSSM-30S, and FSSM-10S before and after high-temperature exposure. Before exposure to high temperatures, absorbance peaks were detected regarding distinct substances as displayed in Fig. 9: the stretching of the O–H bond in CH was respected to the wavenumber near 3640 cm^{-1} [43], the peak ranging from 1200 to 1400 cm^{-1} was connected to the bending mode of CO_3 [44], the limited peak at approximately 1100 cm^{-1} was allocated to the stretching of SO_4 in monosulphate (AFm) or ettringite [45], and the peak ranging from 960 to 1000 cm^{-1} was contributed to the stretching of Si–O bond in C–S–H or SiO_2 [46], and the cramped peak ranging from 820 to 880 cm^{-1} was for another dissymmetry stretching of CO_3 [44]. In this section, the peak (960–1000 cm^{-1}) variation was assumed to be mainly caused by C–S–H since quartz (SiO_2) could stabilize after exposure to 700 °C [29]. Before being exposed to high temperatures, the signals from Fig. 12(a) for AFt/AFm and C–S–H were slightly substantial in FSSM than in FRRM, which confirmed the superior extent hydration of mortars with seawater and sea sand than those mortars mixed with river sand and distilled water. There were no significant differences in the signals from Fig. 9(b) between FSSM and FSSM-1F, demonstrating that the fiber did not affect the hydration reaction. When the addition of GGBFS was increased, the signals from Fig. 9(c) and (d) for AFt/AFm and C–S–H could notably be increased, but $Ca(OH)_2$ could be apparently decreased, which confirmed that more gel materials could be formed through the pozzolanic reaction of cement.

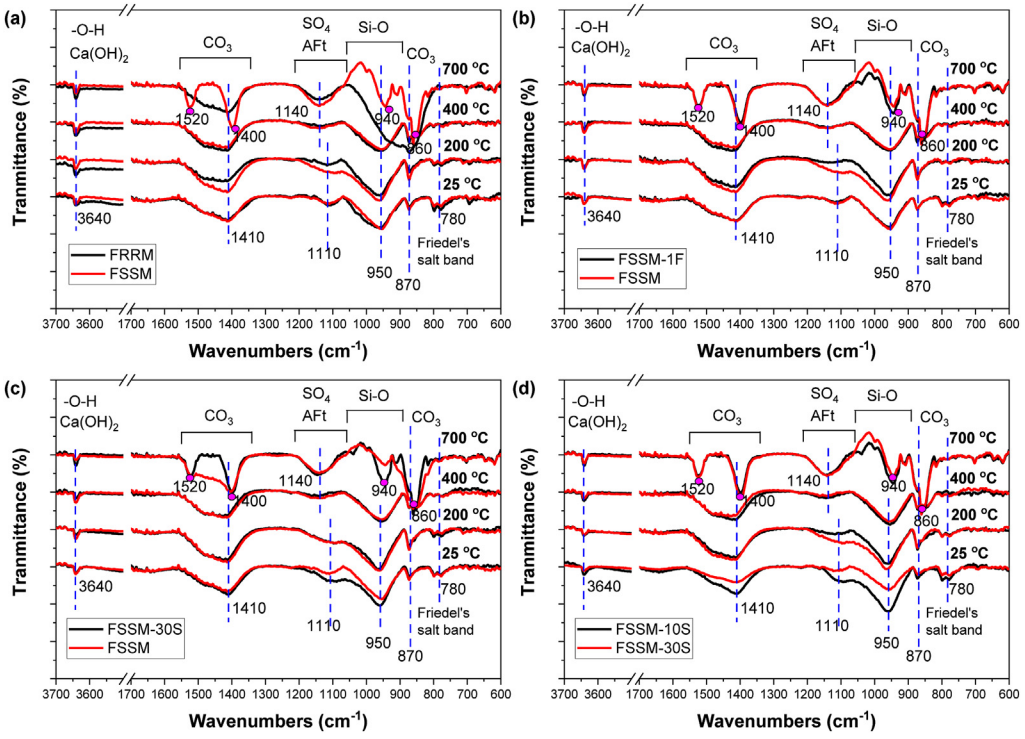

Fig. 9 – FTIR analysis on mortars before and after high-temperature exposures: (a), FRRM and FSSM; (b), FSSM and FSSM-1F; (c), FSSM and FSSM-30S; and (d), FSSM-30S and FSSM-10S.

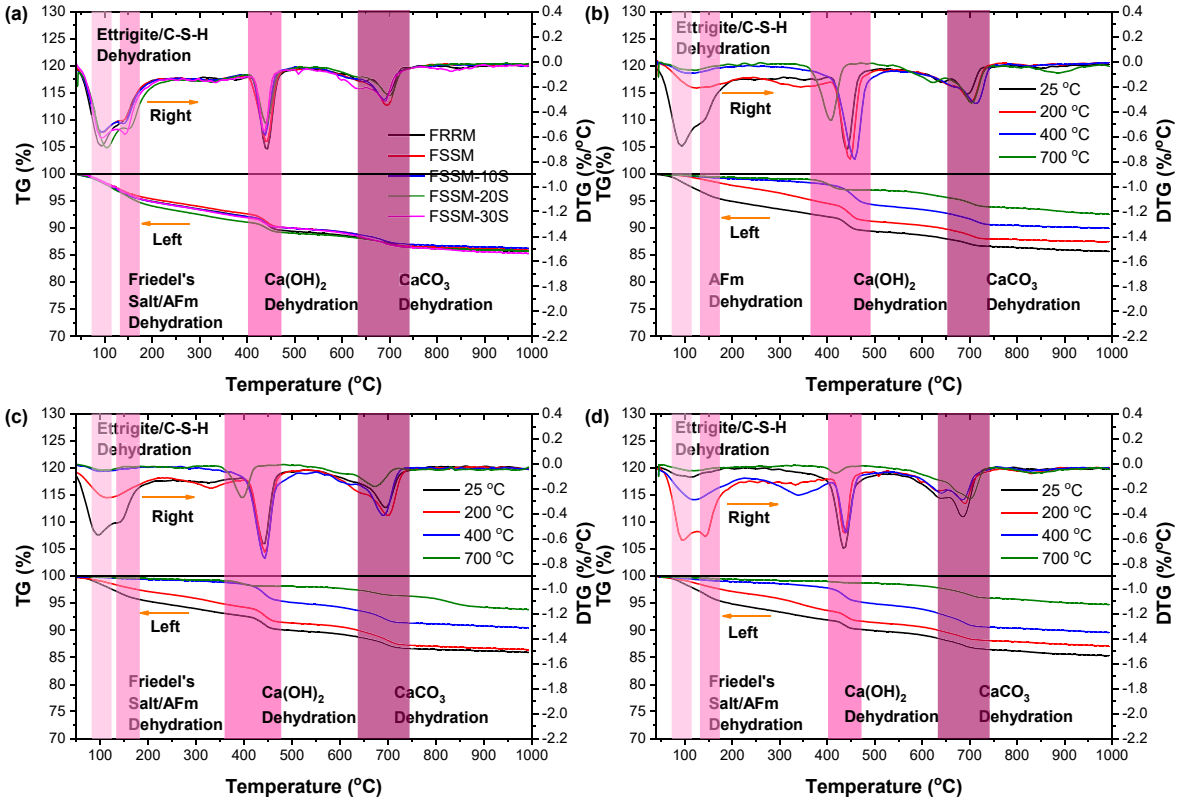

Fig. 10 – TG and DTG analysis of mortars before and after high-temperature exposures: (a), Comparison at 25 °C; (b), FRRM; (c), FSSM and (d), FSSM-30S.

After exposure to 200 °C, there was a reduction in the peak of AFt/AFm and C–S–H among all specimens. The chemical bounded water from AFt/AFm, and C–S–H could indeed be decomposed after being exposed to this temperature [29]. The differences of these peaks were enlarged among FRRM and FSSM groups, which were related to a denser microstructure in the FSSM. The signals for AFt/AFm and C–S–H in the FSSM-GGBFS group with a high content of GGBFS were also higher than those in the FSSM group. At a temperature of 400 °C, the narrow peaks of all specimens around 1100 cm^{-1} was gradually disappeared, which indicated that almost all AFt/AFm were mostly decomposed. The peak of C–S–H for all groups was also reduced as the increasing exposure temperature. The differences in the C–S–H peak were narrowed among all groups. When the temperature reached 700 °C, there was a sharp reduction in the peak of C–S–H among all groups. The peak of C–S–H could still be detected in the FSSM, FSSM-F, and FSSM-GGBFS group, compared to no obvious peck of C–S–H detected in the FRRM, which indicated that higher stable microstructure in 700 °C could be founded in FSSM. Besides, the change of the C–S–H peak was also lower in FSSM-30S than FSSM-10S, demonstrating that the addition of GGBFS could also enhance the stable microstructure of FSSM.

4.3.3. *Thermogravimetric analysis*

Thermogravimetric analyses were conducted on powder samples to evaluate the alterations of the hydration reaction products for mortars before and after high-temperature exposure. Fig. 10(a) shows the comparative thermogravimetry (TG) and derivative thermogravimetry (DTG) results of mortar specimens before high-temperature exposure. As shown by the XRD and FTIR results above, TGA results for the specimens with fibers were not shown in this section because no significant differences were founded between the corresponding mixtures with or without glass fibers. According to the DTG results, two narrow peaks in FRRM could be detected approximately ranging from 100 °C to 200 °C, which was mainly caused by the loss of free water and the dehydration of ettringite, C–S–H, and AFm [47–51], while two small peaks in the group with seawater and sea sand could be found in the same temperature range owing to the dehydration of ettringite, C–S–H, AFm, and Friedel's salt [36,52]. The FSSM-GGBFS group had the most massive intensity of the AFm dehydration peak, followed by the FSSM and FRRM group, which might have something to do with the sulfate content in seawater and sea sand. A noticeable sharp peak between 450 °C and 500 °C, attributed to the dehydration of $Ca(OH)_2$, occurred in all specimens [53]. Another peak, primarily due to the

decomposition of $CaCO_3$, was founded around 720 °C [54]. Compared to the FRRM group, the intensity of the CH dehydration peak was much lower in the FSSM group and decreased in the FSSM-GGBFS group with the increasing GGBFS content, which was contributed to the consumption of $Ca(OH)_2$ by the hydration reaction of ions in seawater/sea sand and the pozzolanic reaction of GGBFS, respectively [42,55]. In the FSSM-GGBFS, the intensity of the decomposition peak of $CaCO_3$ was lower than that in the FSSM, which indicated that fewer $CaCO_3$ existed in the FSSM-GGBFS.

Fig. 10(b)–(d) shows the TG and DTG comparison of FRRM, FSSM, and FSSM-30S before and after the high-temperature exposure. After exposure to 200 and 400 °C, there was an apparent decrease in the intensity of the peak around 200 °C for all mixes in the DTG curves, while there was no noticeable change for the CH and dehydration peaks, which indicated that the decomposition of the AFt, AFm and Friedel's salts primarily accounted for the strength loss after exposure to these temperatures. Besides, the evaporation of some chemically bounded water and the C–S–H gels' shrinkage could also be increased as the increasing high temperature, partially leading to the strength loss after exposure to these temperatures [47]. However, after exposure to 700 °C, except for those peaks close to 200 °C in the DTG curve, the CH dehydration peak in all mixtures decreased significantly, and the carbonate dehydration also decreased slightly, which might lead to a lower strength reduction in all mixes after exposure to this temperature. In addition, weight changes mainly related to the evaporation of chemically bonded water in the tested samples between 200 °C and 1000 °C were also presented in Table 4. From Table 4, it could be known that the evaporation of chemically bonded water in the FSSM group was higher than the FRRM group after being exposed to all different elevated temperatures and could be increased by the addition of GGBFS. Besides, the decomposition of C–S–H had been confirmed [56–58] to begin when the exposure temperature is over 500 °C, and it would lead to a noticeable alteration in the pore structure of the mortar matrix. Thus, the gels' distinct decomposition procedure after exposure to 700 °C also led to the incompatible strength loss in all specimens.

4.3.4. *BSE with energy dispersive X-ray*

Fig. 11(a)–(d) shows the BSE morphologies with the EDX results of FRRM, FSSM, FSSM-1F, and FSSM-30S mixes at different temperatures. Before high-temperature exposure in Fig. 11(a1)–(d1), the BSE morphologies of all specimens were generally dense. The detected EDX results of C–S–H in FRRM and Friedel's salts in FSSM and FSSM-30S corresponded to the XRD results mentioned in Fig. 8. Besides, the existence of glass fibers was confirmed by the EDX results with high intensity of the Si and Na because the primary chemical component of glass fibers was sodium silicate. In Fig. 11(c1), a poor fiber–paste interface along the longitudinal might explain a lower compressive strength in the group with fibers than those without fibers. When the exposure temperature reached 200 °C in Fig. 11(a2)–(d2), some small pores were detected in the FRRM and FSSM, compared to a relative dense microstructure detected in FSSM-1F and FSSM-30S, which suggested that the increased content of glass fiber and GGBFS could improve the fire resistivity of the FSSM group. The EDX results of CH could be detected in all mixes. The microstructure changes in these mixtures were mainly related to the evaporation of the free water, AFm/AFt under this temperature, consistent with the XRD and FTIR results. Besides, most of the glass fibers in FSSM-1F could be detected, which confirmed the unchanged mass of the fiber shown in Fig. 2.

After exposure to 400 °C, in addition to the existence of inevitable pores, the cracks alone the weak interface between the river sand and paste matrix in FRRM could be observed, while only some small pores could be detected in FSSM, FSSM-1F, and FSSM-30S group. This indicated that the mortars mixed with seawater and sea sand could perform better than the mortars with river sand and demineralized water. C–S–H gels were examined in all specimens, demonstrating that C–S–H could be stable after exposure to 400 °C. Besides, the relatively complete glass fibers were still able to be recorded in the FSSM-1F, confirming 20% mass loss of fiber in Fig. 2. Fewer cracks were generated in FSSM-1F, and spalling could be prevented in FSSM-1F in the contract to these groups without glass fibers. After exposure to 700 °C, it seemed that with the increasing exposure temperatures, fibers were nearly melted (nearly 80% mass loss shown in Fig. 2) and left channels, which could release the internal pressure in the mortar matrix, as shown in Fig. 11(c4). In addition, more substantial cracks in the FRRM group and apparent cracks in the FSSM group along the weak interface could also be presented in the BSE morphologies. However, some pores were detected in FSSM-30S, which confirmed that adding GGBFS could enhance the microstructure of seawater and sea-sand mortars. The calcium aluminosilicate hydrate (C–A–S–H) could also be detected in the FSSM-30S group even after being exposed to 700 °C. The combination of GGBFS and fiber made a more stable microstructure in the FSSM-GGBFS-F group, even after exposure to 700 °C. Besides, Fig. 12 displays the BSE maps of FSSM-1F before and after high-temperature exposure. The main chemical composition of glass fibers was Na_2SiO_3. There were nearly no detected elements of Na after exposure to 700 °C, which also confirmed that most of the glass fibers were melted after exposure to 700 °C.

In order to evaluate the phase change, the EDX point analysis for the primary elements (Al, Ca, Cl, and Si) in a volume of approximately 1 μm^3 was adopted. The results were displayed in ratios lying in between the best possible stoichiometry of these phases [59,60]. Fig. 13(a) and (b) present the Al/Ca ratio as a function of the Si/Ca ratio for FRRM, FSSM, and FSSM-30S before high-temperature exposure and exposure to a temperature of 700 °C, respectively. C–S–H/C–A–S–H was expressed by a dotted circle. Before high-temperature exposure, compared to the FRRM group, the Si/Ca and Al/Ca ratios of the C–S–H were higher in the FSSM group, which might be

Table 4 – Weight loss of mortar before and after high-temperature exposures (200–1000 °C).

Specimen	Weight loss (%)			
	25 °C	200 °C	400 °C	700 °C
FRRM	10.1	9.2	8.9	4.7
FSSM	10.4	9.4	9.0	5.8
FSSM-30S	10.8	9.6	9.4	6.7

caused by the ions content in seawater or sea sand [36]. The addition of GGBFS could also increase the Si/Ca and Al/Ca ratios of the C–S–H in FSSM. The Si/Ca ratio of C–A–S–H in FSSM-30S was around 0.6–0.8, and the Si/Ca ratio of C–S–H in FSSM was about 0.5–0.7, in contrast to the Si/Ca ratio in FSSM-30S around 0.4–0.6. After exposure to 700 °C, the Si/Ca ratio of C–S–H in FRRM could be decreased to around 0.4–0.5 as the high temperature increased. There were sight changes in the Si/Ca ratio of C–S–H from 0.5–0.7 to 0.5–0.65. No significant changes of Si/Ca and Al/Ca ratios of C–A–S–H in the FSSM-30S group were founded, which might be to the chain length of C–A–S–H gels [61]. The long-chain length would make the C–A–S–H gels more thermally stable after high-temperature exposure [61].

Fig. 13(c) and (d) presented the Cl/Ca ratio as a function of the Al/Ca ratio for FRRM, FSSM, and FSSM-30S before exposure to high temperature and exposure to a temperature of 700 °C, respectively, which also showed the ideal

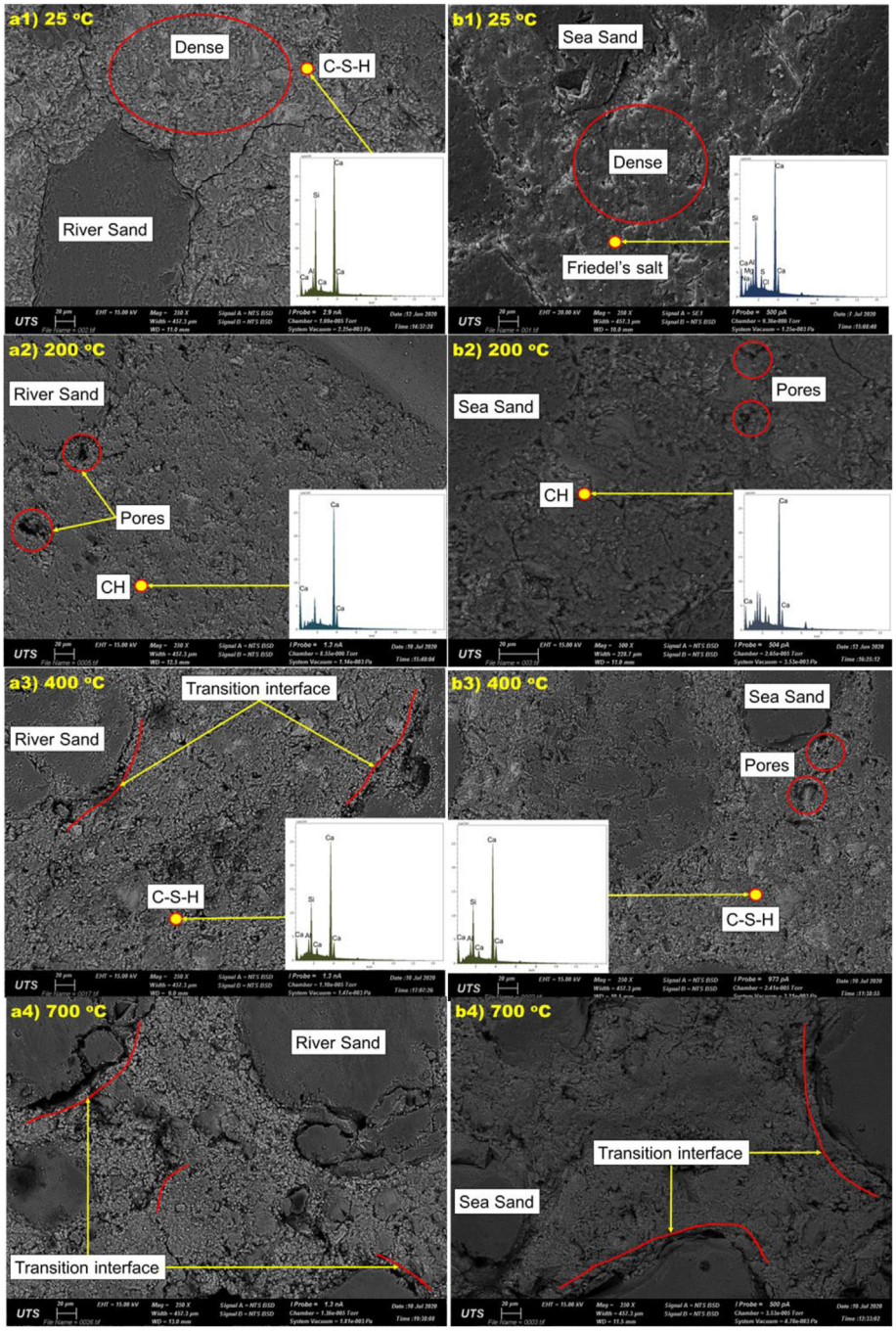

(a) FRRM and (b) FSSM

Fig. 11 – Characterization using BSE-EDX (250 magnification) before high-temperature exposure for mixes.

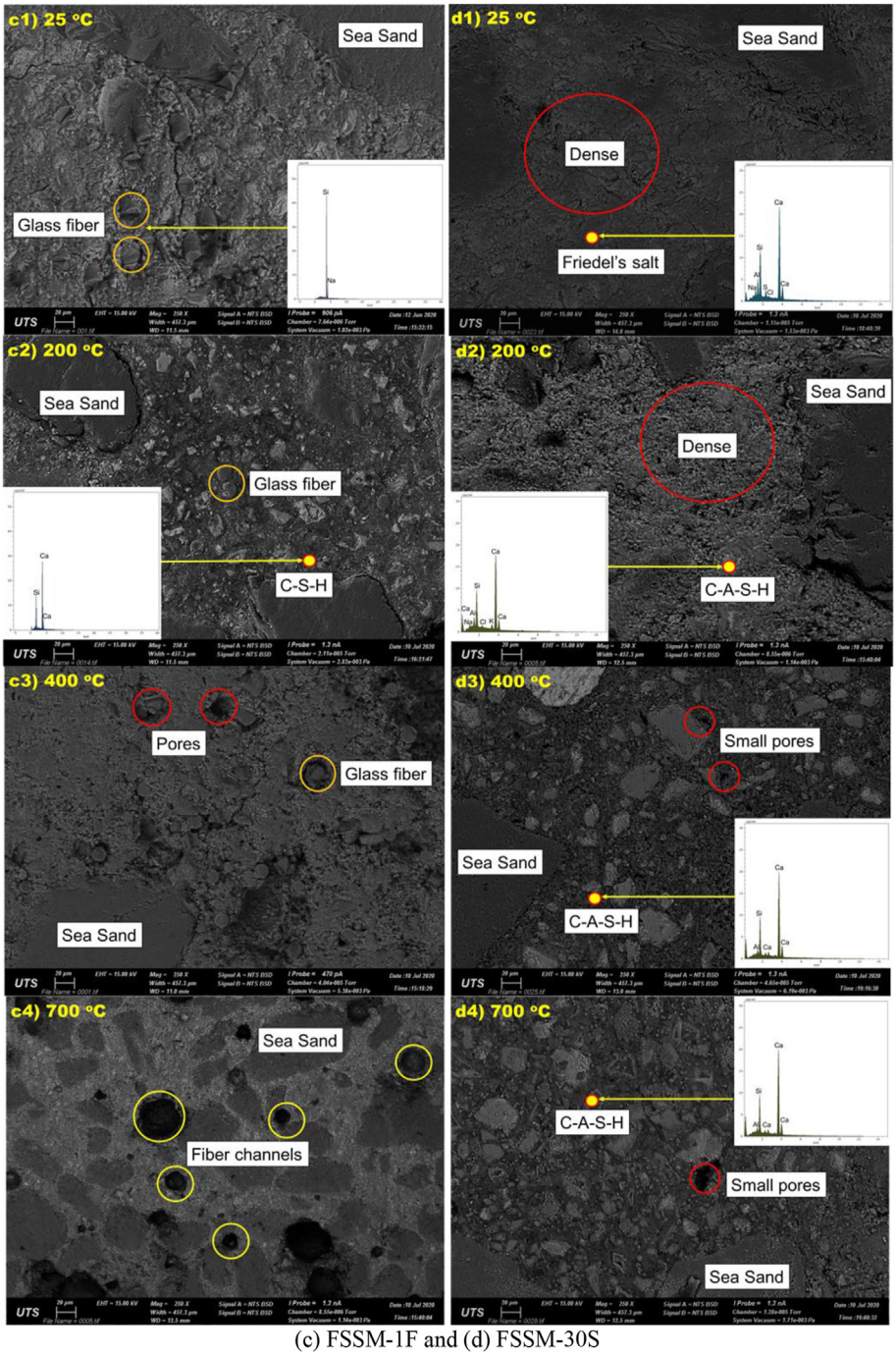

(c) FSSM-1F and (d) FSSM-30S

Fig. 11 – *(continued)*.

stoichiometry of the Friedel's salt, AFm, and AFt phases. Before exposure to high temperature, the AFt could be examined in the FRRM, while no chloride content was detected in the FRRM. Friedel's salts could be examined in the FSSM, while the AFm could not be recorded in the FSSM. The AFm could be detected in the FSSM-30S. These points in Fig. 13(c), located in the 0.0–0.1 Al/Ca and 0.1–0.25 Cl/Ca molar ratio range in FSSM, were supposed to stand for chlorides adsorbed on the C–S–H. Besides, a number of points, located in the 0.4–0.6 Al/Ca and 0.1–0.25 Cl/Ca molar ratio range in FSSM-30S, were assumed to represent chlorides adsorbed on the C–A–S–H. This might indicate that the ability to absorb chlorides of C–A–S–H could be higher than that of C–S–H. After exposure to a temperature of 700 °C, Friedel's salt could hardly be detected in the FSSM, which indicated that the decomposition of Friedel's salt could occur at a high temperature. In addition, no significant Cl/Ca ratio changes in FSSM-30S and slight Cl/Ca ratio changes in FSSM were found, which indicated that the

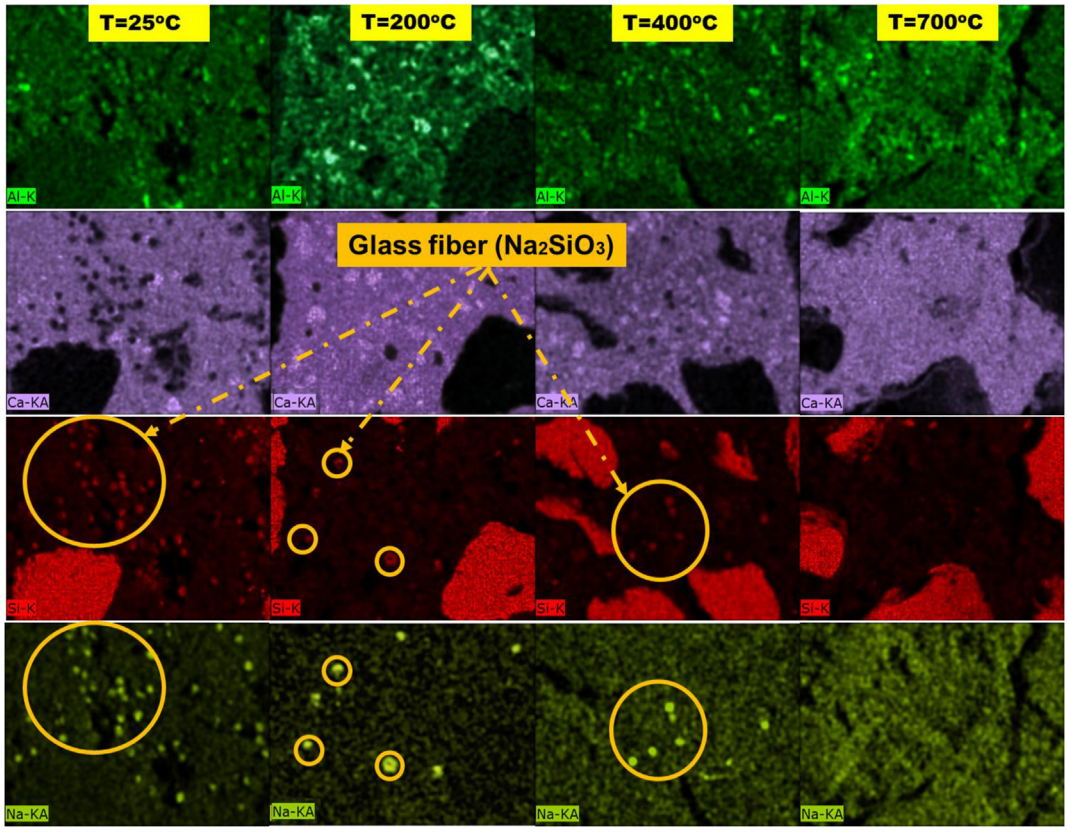

Fig. 12 – Element analysis of FSSM with glass fiber before and after the high-temperature exposure.

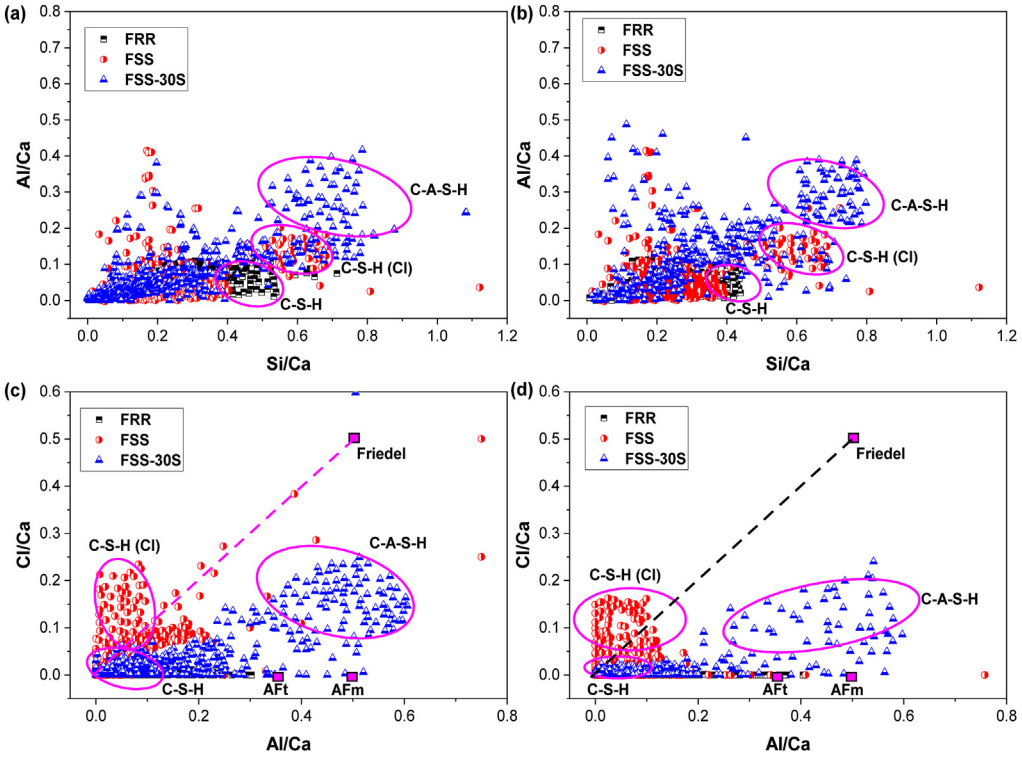

Fig. 13 – BSE-EDX analysis of FRRM, FSSM and FSSM-30S before and after high-temperature exposure: (a), Al/Ca as a function of Si/Ca (at 25 °C); (b), Al/Ca as a function of Si/Ca (at 700 °C); (c), Cl/Ca as a function of Al/Ca (at 25 °C); and (d), Cl/Ca as a function of Al/Ca (at 700 °C). Note: C–S–H, C–S–H (Cl), and C–A–S–H were used to distinguish the gels in FRRM, FSSM, and FSSM-30S, respectively.

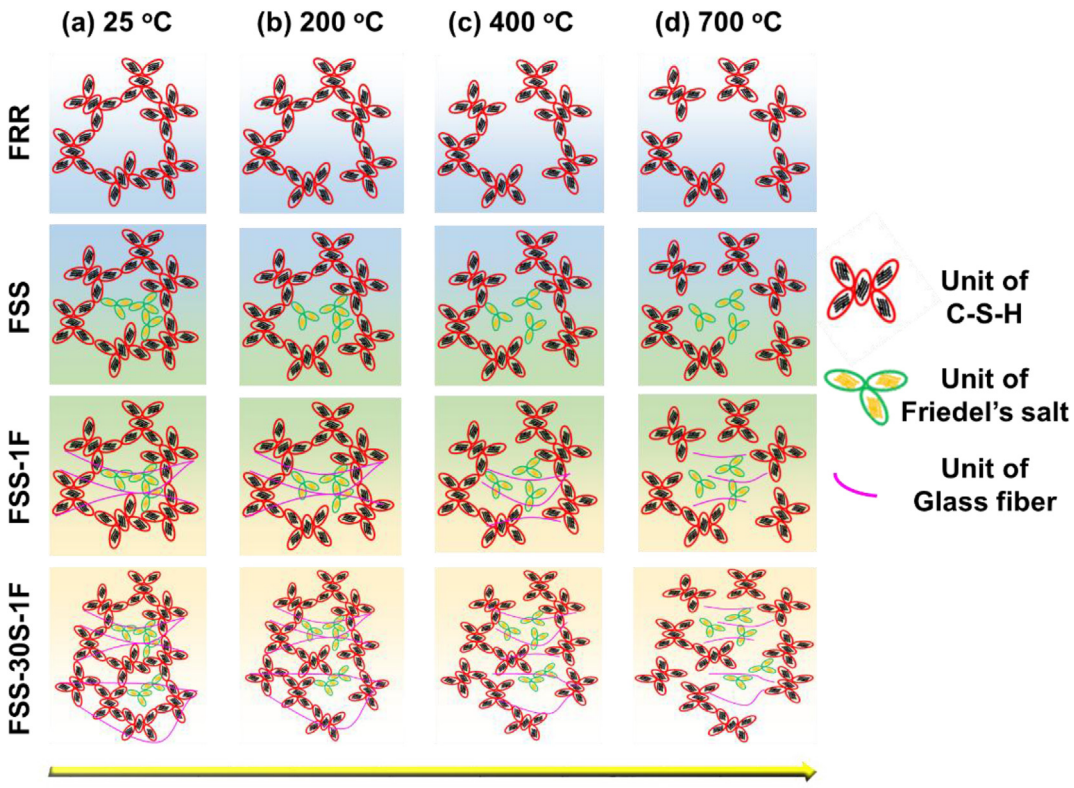

Fig. 14 – Schematically diagrams for the microstructure change of the binder gels before and after high-temperature exposure.

C–A–S–H in FSSM-30S was relatively stable than that of C–S–H gels (Cl) in FSSM.

4.4. *Mechanism discussions*

As mentioned above, alterations in the microstructure of hydration products could be seen among the different mortar mixtures after high-temperature exposure, which might have contributed to the microstructural change in binder gels, including Friedel's salt and C–S–H. By comparing the results mentioned above, a diagram for the microstructure evolutions of the binder gels before and after high-temperature exposure is schematically drawn in Fig. 14. The diagrams for FSSM, FRRM, FSSM-1F and FSSM-30S-1F are drawn in Fig. 14, primarily displaying the effect of seawater, sea sand, fiber, and GGBFS. The mechanism of fire resistivity seems to be different for different specimens.

Before the high-temperature exposure, the salt content (mainly chloride) in seawater and sea sand could accelerate the cement hydration with more hydrates produced, including Friedel's salt in FSSM (see Fig. 8) [36], resulting in more stable gels structures in the FSSM group than in FRRM group shown in Fig. 14, which could explain a higher compressive strength was founded in FSSM from Fig. 6. Though the mean chain length of binder gels in FRRM was normally the same as FSSM, Friedel's salt could make the binder gels more stable. In Fig. 14, with the addition of the glass fiber, the bridging effect between the mortar matrix and glass fiber would prevent micro-cracking formation with increased tensile strength. Thus, there was a high flexural strength detected in the FSSM-1F group in Fig. 6. As the results of the incorporation of GGBFS, the high aluminum content of the FSSM-30S group is higher than that of groups without GGBFS content [62]. These changes could be attributed to the pozzolanic reaction between GGBFS and $Ca(OH)_2$. The corporation of GGBFS could optimize the composition and microstructure of C–S–H [47]; thus, the C–S–H gels in the FSSM group with GGBFS were also called C–A–S–H gels [63]. The incorporation of glass fiber and GGBFS could provide a more stable microstructure with a longer mean chain length (see Fig. 14) in the FSSM-30S-1F group, with the highest flexural strength in the FSSM-1F-30S.

At the temperature of 200 °C, the proportion of C–S–H in Figs. 8 and 9 barely displayed noticeable variations, but in Fig. 12, a pronounced reduction of the peak around 100–200 °C in the TGA curves was detected with a slight decreasing strength founded in Fig. 7. In addition, there was a reduction in the peak of Friedel's salt from Fig. 10 in all mixes with seawater and sea sand. The significant friction of free water evaporation and small friction of chemical bounded water evaporation would mainly explain the small change of the gel's microstructure for most mixes (Fig. 14). At this temperature, the glass fiber could perform well, as confirmed in Figs. 2 and 12. Thus, there was only a small flexural strength loss in the group with fiber. Friedel's salt could be partially decomposed and the glass fiber could be relatively stable, as shown in Fig. 14. When the temperature was up to 400 °C, the similar results about the microstructure of the C–S–H and other

phases were founded corresponded with those found at 200 °C, except for the partially melted glass fiber detected in Fig. 12. Therefore, a more significant flexural strength loss was founded in all mixes. Due to a denser microstructure in the FSSM group, there was less strength loss in FSSM than in FRRM, which accounted for a higher flexural strength from Fig. 6 in FSSM than in FRRM. The fineness modulus and physical properties of the sea sand could have an adverse effect on the flexural strength behavior, but the microstructure of all specimens would play a critical role in the mortars' fire resistivity. Friedel's salt could be further decomposed, and the glass fiber could be partially melted, as shown in Fig. 14.

After exposure to 700 °C, C–S–H in FRRM, FSSM, and FSSM-1F mixtures had already decomposed according to the XRD results, which could cause the collapse of the gel structure. In addition, the C–S–H gels also endured shrinkage at elevated temperatures with a reduction in the packing density of C–S–H [64], which caused great damages to the gel's structure. The glass fiber could also entirely be melted after being exposed to 700 °C. Therefore, the flexural strength loss of FRRM, FSSM, and FSSM-1F group could up to be 100% showed in Fig. 7. The gels structure of FRRM, FSSM, and FSSM-1F could be all destroyed, as shown in Fig. 14. Previous studies on the high-temperature stability of C–S–H presented that C–S–H with higher Si/Ca was more stabilizing at the elevated temperatures, possibly contributing to the silicate microstructure [65]. On the basis of the EDX results, the C–A–S–H in the FSSM-30S had higher ratios of Si/Ca and Al/Si in contrast to the C–S–H in the mixtures without GGBFS or with low GGBFS content (see Fig. 13). It was generally considered that the average chain length of C–S–H is shorter than C–A–S–H [61]. Thus, the high Si/Ca and distinct chain microstructure possibly caused the C–A–S–H gels to be more stabilizing than C–S–H gels at elevated temperatures. The C–A–S–H gels in the group with GGBFS could still cover familiarly after high-temperature exposure in the BSE result. In Fig. 11, the BSE-EDX result illustrated that the C–A–S–H gels in the FSSM-30S group remained high even if the exposure temperature arrives at 700 °C, which possibly indicated that component of C–A–S–H gels could also protect the gel structure from deteriorating even at elevated temperature, further identifying the stability of C–A–S–H gels. The C–A–S–H gels also endured shrinkage at elevated temperatures, leading to a 100% flexural strength loss in the FSSM-GGBFS group. However, the thermal stable gel's structure would protect the glass fiber from being melted, which would make the most stable gel's structure in the FSSM-GGBFS-F group and lead to a comparatively small flexural strength loss in the FSSM-GGBFS-F (see Fig. 14).

In terms of fire or high-temperature resistance, the increasing addition of GGBFS could stabilize the microstructure of FSSM. However, the flexural strength loss of the FSSM-GGBFS group could still be up to 100%. Combining the additions of GGBFS and fiber, the FSSM-GGBFS-F group performed well with high flexural strength and low flexural strength loss after high-temperature exposure. In this study, FSSM-30S-1F achieved the best fire or high-temperature resistance.

5. Conclusions

The effects of GGBFS and glass fiber on the mechanical properties, high temperature resistance and microstructure of seawater sea sand mortars after exposed to elevated temperatures were investigated in this study. The related conclusions could be drawn up as below:

(1) Before exposed to high temperature, compared with FRRM, the ion content (mainly chloride) in seawater sea sand reacting with cement particles increased the compressive strength of FSSM, while sea sand with lower fineness modulus and reduced flexural strength. The glass fiber could improve the flexural strength of FSSM, but the porous microstructures around the fiber–paste interfaces could reduce the compressive strength. The GGBFS could increase both the flexural and compressive strengths of FSSM due to the pozzolanic reaction, but the compressive strength of the FSSM with GGBFS and glass fiber was still lower than that of the FSSM with only GGBFS.

(2) After exposed to the high temperatures of 400 °C and 700 °C, compared with FRRM, the accelerated hydration reaction caused by salt densified the microstructure of FSSM, thereby reducing the mass loss, strength loss and cracking. Glass fibers could be partially and mostly melted after exposed to the temperatures of 400 °C and 700 °C, respectively, which clearly increased the losses of mass and compressive strength of FSSM. Glass fibers could also effectively prevent the formation of cracks caused by high-temperature exposure and further decrease the flexural strength loss for FSSM.

(3) GGBFS could densify the microstructures of FSSM and decrease the strength loss caused by high-temperature exposure. The increased content of GGBFS could decrease crack formation, while both longitudinal and transverse cracks were still found in the FSSM only with GGBFS. The combination of the GGBFS and glass fibers could improve the fire resistivity of the FSSM. After exposed to 700 °C, FSSM with GGBFS and glass fibers still exhibited certain flexural strength and few visible cracks on the surface.

(4) Chloride ions in seawater and sea sand could accelerate the hydration reaction of cement and produce the Kuzel's and Friedel's salt. The decomposition of AFt, AFm and Friedel's salts primarily accounted for the hydration product changes after exposed to 200 °C and 400 °C. Glass fiber almost had no effect on cement's hydration reaction, while the bridging effect between the cement matrix and glass fiber could prevent the micro-crack formation.

(5) GGBFS could optimize the composition and densify the microstructure of FSSM. The Si/Ca ratio of FSSM without GGBFS decreased after high-temperature exposure, while the Si/Ca ratios of the FSSM with GGBFS almost maintained constant. C–A–S–H gels in the FSSM with GGBFS were much more stable than that of C–S–H. Because the increased addition of GGBFS promoted C–A–S–H gels'

formation packed along the glass fibers, the fire resistivity of FSSM with glass fibers and GGBFS was improved. The best high-temperature resistivity was achieved for FSSM with 30% GGBFS and 1% glass fibers by weight.

Declaration of Competing Interest

The authors declare that they have no known competing financial interests or personal relationships that could have appeared to influence the work reported in this paper.

Acknowledgments

The authors appreciate the supports from the Australian Research Council (ARC) (DE130101751; IH150100006 and IH200100010), University of Technology Sydney Research Academic Program at Tech Lab (UTS RAPT), and University of Technology Sydney Tech Lab Blue Sky Research Scheme. The first author also appreciates the support from the China Scholarship Council (CSC) scholarship.

REFERENCES

[1] Wang HY. A study of the effects of LCD glass sand on the properties of concrete. Waste Manag 2009;29(1):335–41.
[2] Qu FL, Li WG, Dong WK, Tam VW, Yu T. Durability performance deterioration of concrete under marine environment from material to structure: a critical review. J Build Eng 2020:102074.
[3] Zhou A, Chow CL, Lau D. Structural behavior of GFRP reinforced concrete columns under the influence of chloride at casting and service stages. Compos B Eng 2018;136:1–9.
[4] Li Y, Teng J, Zhao X, Raman RS. Theoretical model for seawater and sea sand concrete-filled circular FRP tubular stub columns under axial compression. Eng Struct 2018;160:71–84.
[5] Ahmed A, Guo S, Zhang Z, Shi C, Zhu D. A review on durability of fiber reinforced polymer (FRP) bars reinforced seawater sea sand concrete. Constr Build Mater 2020;256:119484.
[6] Carabba L, Pirskawetz S, Krüger S, Gluth GJ, Bignozzi MC. Acoustic emission study of heat-induced cracking in fly ash-based alkali-activated pastes and lightweight mortars. Cement Concr Compos 2019;102:145–56.
[7] Manjunath R, Narasimhan MC, Umesha K. Studies on high performance alkali activated slag concrete mixes subjected to aggressive environments and sustained elevated temperatures. Constr Build Mater 2019;229:116887.
[8] Liu D, Xu Z, Zhou Y, Fan C. Heat map visualisation of fire incidents based on transformed sigmoid risk model. Fire Saf J 2019;109:102863.
[9] Nguyen KT, Navaratnam S, Mendis P, Zhang K, Barnett J, Wang H. Fire safety of composites in prefabricated buildings: from fibre reinforced polymer to textile reinforced concrete. Compos B Eng 2020;187:107815.
[10] Fernandes B, Gil AM, Bolina F, Tutikian BF. Microstructure of concrete subjected to elevated temperatures: physico-chemical changes and analysis techniques. Rev IBRACON Estrut Mater 2017;10(4):838–63.
[11] Zhang P, Zheng Y, Wang K, Zhang J. A review on properties of fresh and hardened geopolymer mortar. Compos B Eng 2018;152:79–95.
[12] Horszczaruk E, Sikora P, Cendrowski K, Mijowska E. The effect of elevated temperature on the properties of cement mortars containing nanosilica and heavyweight aggregates. Constr Build Mater 2017;137:420–31.
[13] Khaliq W, Mujeeb A. Effect of processed pozzolans on residual mechanical properties and macrostructure of high-strength concrete at elevated temperatures. Struct Concr 2019;20(1):307–17.
[14] Shaikh F, Taweel M. Compressive strength and failure behaviour of fibre reinforced concrete at elevated temperatures. Adv Concr Constr 2015;3(4):283–93.
[15] Zaidi K, Sharma U, Bhandari N. Effect of temperature on uni-axial compressive behavior of confined concrete. Fire Saf J 2012;48:58–68.
[16] Erdogmus E. Use of fiber-reinforced cements in masonry construction and structural rehabilitation. Fibers 2015;3(1):41–63.
[17] Al MS, Bakhsh EM, Tonguc B, Khan SB. Mechanical and radiation shielding properties of tellurite glasses doped with ZnO and NiO. Ceram Int 2020;46(11):19078–83.
[18] Al MS, Tonguç B, Perişanoğlu U, Kavaz E. The impact of Gd_2O_3 on nuclear safety proficiencies of TeO_2–ZnO–Nb_2O_5 glasses: a GEANT4 Monte Carlo study. Ceram Int 2020;46(15):23347–56.
[19] Boukhris I, Kebaili I, Al MS, Alalawi A, Abouhaswa A, Tonguc B. Photon and electron attenuation parameters of phosphate and borate bioactive glasses by using Geant4 simulations. Ceram Int 2020;46(15):24435–42.
[20] Al MS, Somaily H, Alalawi A, Alraddadi S. Polarizability, optical basicity, and photon attenuation properties of Ag_2O–MoO_3–V_2O_5–TeO_2 glasses: the role of silver oxide. J Inorg Organomet Polym Mater 2021;31(3):1047–56.
[21] Kizilkanat AB, Kabay N, Akyüncü V, Chowdhury S, Akça AH. Mechanical properties and fracture behavior of basalt and glass fiber reinforced concrete: an experimental study. Constr Build Mater 2015;100:218–24.
[22] Mazaheripour H, Barros JA, Sena J, Pepe M, Martinelli E. Experimental study on bond performance of GFRP bars in self-compacting steel fiber reinforced concrete. Compos Struct 2013;95:202–12.
[23] Kavas T, Sabah E, Çelik M. Structural properties of sepiolite-reinforced cement composite. Cement Concr Res 2004;34(11):2135–9.
[24] Bertelsen I, Ottosen L, Fischer G. Influence of fibre characteristics on plastic shrinkage cracking in cement-based materials: a review. Constr Build Mater 2020;230:116769.
[25] Güllü A, Özdemir A, Özdemir E. Experimental investigation of the effect of glass fibres on the mechanical properties of polypropylene (PP) and polyamide 6 (PA6) plastics. Mater Des 2006;27(4):316–23.
[26] Keleştemur O, Arıcı E, Yıldız S, Gökçer B. Performance evaluation of cement mortars containing marble dust and glass fiber exposed to high temperature by using Taguchi method. Constr Build Mater 2014;60:17–24.
[27] Fang Y, Cui P, Ding Z, Zhu JX. Properties of a magnesium phosphate cement-based fire-retardant coating containing glass fiber or glass fiber powder. Constr Build Mater 2018;162:553–60.
[28] Dulaimi A, Shanbara HK, Al-Rifaie A. The mechanical evaluation of cold asphalt emulsion mixtures using a new cementitious material comprising ground-granulated blast-furnace slag and a calcium carbide residue. Constr Build Mater 2020;250:118808.

[29] Qu FL, Li WG, Tao Z, Castel A, Wang KJ. High temperature resistance of fly ash/GGBFS-based geopolymer mortar with load-induced damage. Mater Struct 2020;53(4):1–21.
[30] Mehta A, Siddique R. Sustainable geopolymer concrete using ground granulated blast furnace slag and rice husk ash: strength and permeability properties. J Clean Prod 2018;205:49–57.
[31] Aziz IH, Abdullah MMAB, Salleh MM, Azimi EA, Chaiprapa J, Sandu AV. Strength development of solely ground granulated blast furnace slag geopolymers. Constr Build Mater 2020;250:118720.
[32] Bernal SA, de Gutierrez RM, Provis JL, Rose V. Effect of silicate modulus and metakaolin incorporation on the carbonation of alkali silicate-activated slags. Cement Concr Res 2010;40(6):898–907.
[33] Aziz IH, Abdullah MMAB, Salleh MM, Yoriya S, Chaiprapa J, Rojviriya C, et al. Microstructure and porosity evolution of alkali activated slag at various heating temperatures. J Mater Res Technol 2020;9(6):15894–907.
[34] Delhomme F, Ambroise J, Limam A. Effects of high temperatures on mortar specimens containing Portland cement and GGBFS. Mater Struct 2012;45(11):1685–92.
[35] Gao D, Yan D, Li X. Splitting strength of GGBFS concrete incorporating with steel fiber and polypropylene fiber after exposure to elevated temperatures. Fire Saf J 2012;54:67–73.
[36] Li PR, Li WG, Yu T, Qu FL, Tam VW. Investigation on early-age hydration, mechanical properties and microstructure of seawater sea sand cement mortar. Constr Build Mater 2020;249:118776.
[37] Ozer-Erdogan P, Basar HM, Erden I, Tolun L. Beneficial use of marine dredged materials as a fine aggregate in ready-mixed concrete: Turkey example. Constr Build Mater 2016;124:690–704.
[38] Kucche K, Jamkar S, Sadgir P. Quality of water for making concrete: a review of literature. Int J Sci Res Publ 2015;5(1):1–10.
[39] Etxeberria M, Fernandez JM, Limeira J. Secondary aggregates and seawater employment for sustainable concrete dyke blocks production: case study. Constr Build Mater 2016;113:586–95.
[40] Li YL, Zhao XL, Raman RS, Al-Saadi S. Thermal and mechanical properties of alkali-activated slag paste, mortar and concrete utilising seawater and sea sand. Constr Build Mater 2018;159:704–24.
[41] Missemer L, Ouedraogo E, Malecot Y, Clergue C, Rogat D. Fire spalling of ultra-high performance concrete: from a global analysis to microstructure investigations. Cement Concr Res 2019;115:207–19.
[42] Yun CM, Rahman MR, Phing CYW, Chie AWM, Bakri MKB. The curing times effect on the strength of ground granulated blast furnace slag (GGBFS) mortar. Constr Build Mater 2020;260:120622.
[43] Zhang J, Shi C, Zhang Z. Carbonation induced phase evolution in alkali-activated slag/fly ash cements: the effect of silicate modulus of activators. Constr Build Mater 2019;223:566–82.
[44] Zunino F, Boehm-Courjault E, Scrivener K. The impact of calcite impurities in clays containing kaolinite on their reactivity in cement after calcination. Mater Struct 2020;53:1–15.
[45] Ylmén R, Jäglid U, Steenari BM, Panas I. Early hydration and setting of Portland cement monitored by IR, SEM and Vicat techniques. Cement Concr Res 2009;39(5):433–9.
[46] Kapeluszna E, Kotwica Ł, Różycka A, Gołek Ł. Incorporation of Al in CASH gels with various Ca/Si and Al/Si ratio: microstructural and structural characteristics with DTA/TG, XRD, FTIR and TEM analysis. Constr Build Mater 2017;155:643–53.
[47] Jia Z, Chen C, Shi J, Zhang Y, Sun Z, Zhang P. The microstructural change of CSH at elevated temperature in Portland cement/GGBFS blended system. Cement Concr Res 2019;123:105773.
[48] Bahafid S, Ghabezloo S, Duc M, Faure P, Sulem J. Effect of the hydration temperature on the microstructure of Class G cement: CSH composition and density. Cement Concr Res 2017;95:270–81.
[49] Liu M, Zhao Y, Xiao Y, Yu Z. Performance of cement pastes containing sewage sludge ash at elevated temperatures. Constr Build Mater 2019;211:785–95.
[50] AzariJafari H, Amiri MJT, Ashrafian A, Rasekh H, Barforooshi MJ, Berenjian J. Ternary blended cement: an eco-friendly alternative to improve resistivity of high-performance self-consolidating concrete against elevated temperature. J Clean Prod 2019;223:575–86.
[51] Alarcon L, Platret G, Massieu E, Ehrlacher A. The use of thermal analysis in assessing the effect of temperature on a cement paste. Cement Concr Res 2005;35(3):609–13.
[52] Ting MZY, Wong KS, Rahman ME, Joo MS. Mechanical and durability performance of marine sand and seawater concrete incorporating silicomanganese slag as coarse aggregate. Constr Build Mater 2020;254:119195.
[53] He P, Zhang B, Lu JX, Poon CS. A ternary optimization of alkali-activated cement mortars incorporating glass powder, slag and calcium aluminate cement. Constr Build Mater 2020;240:117983.
[54] Zhang Y, Yu P, Pan F, He Y. The synergistic effect of AFt enhancement and expansion in Portland cement-aluminate cement-FGD gypsum composite cementitious system. Constr Build Mater 2018;190:985–94.
[55] De Weerdt K, Justnes H. The effect of sea water on the phase assemblage of hydrated cement paste. Cement Concr Compos 2015;55:215–22.
[56] Zhang Q, Ye G, Koenders E. Investigation of the structure of heated Portland cement paste by using various techniques. Constr Build Mater 2013;38:1040–50.
[57] Kurihara R, Maruyama I. Effects of heating and drying on the strength and stiffness of high-early-strength Portland cement pastes. Cement Concr Compos 2020;106:103455.
[58] Suh H, Jee H, Kim J, Kitagaki R, Ohki S, Woo S, et al. Influences of rehydration conditions on the mechanical and atomic structural recovery characteristics of Portland cement paste exposed to elevated temperatures. Constr Build Mater 2020;235:117453.
[59] De Weerdt K, Justnes H, Geiker MR. Changes in the phase assemblage of concrete exposed to sea water. Cement Concr Compos 2014;47:53–63.
[60] De Weerdt K, Lothenbach B, Geiker MR. Comparing chloride ingress from seawater and NaCl solution in Portland cement mortar. Cement Concr Res 2019;115:80–9.
[61] Puertas F, Palacios M, Manzano H, Dolado J, Rico A, Rodríguez J. A model for the CASH gel formed in alkali-activated slag cements. J Eur Ceram Soc 2011;31(12):2043–56.
[62] Taylor R, Richardson I, Brydson R. Composition and microstructure of 20-year-old ordinary Portland cement–ground granulated blast-furnace slag blends containing 0 to 100% slag. Cement Concr Res 2010;40(7):971–83.
[63] Wei Y, Gao X, Liang S. A combined SPM/NI/EDS method to quantify properties of inner and outer CSH in OPC and slag-blended cement pastes. Cement Concr Compos 2018;85:56–66.

[64] DeJong MJ, Ulm FJ. The nanogranular behavior of CSH at elevated temperatures (up to 700 C). Cement Concr Res 2007;37(1):1–12.

[65] Rodriguez ET, Garbev K, Merz D, Black L, Richardson IG. Thermal stability of CSH phases and applicability of Richardson and Groves' and Richardson C-(A)-SH (I) models to synthetic CSH. Cement Concr Res 2017;93:45–56.